Virtual Source Extended Range Points Migration Method for Auto-Focusing 3-D Terahertz Imaging

Takamaru Matsui and Shouhei Kidera, *Member, IEEE*

***Abstract*— This letter presents an auto-focusing imaging algorithm for terahertz (THz) band imaging by extending the range point migration (RPM) method using a dielectric lens model. The traditional THz time-domain spectroscopy (THz-TDS) imaging system has an essential problem for depth dependence of the azimuth resolution, which becomes more crucial in subsurface imaging, because the depth of target is unknown in most cases. This letter thus introduces an RPM-based auto-focusing imaging method using an equivalent virtual source model to accurately represent both near- and far-range areas from the focal point. Experimental validation using THz-TDS demonstrated that the proposed algorithm accurately compensates image distortions by out-of-focus effect with much lower complexity than traditional radar-imaging approaches.**

***Index Terms*— 3-D imaging, radar signal processing, submillimeter wave, subsurface imaging, synthetic aperture (SA) process, terahertz (THz) wave.**

I. Introduction

RESEARCHERS have demonstrated that 3-D terahertz (THz) imaging systems may offer higher spatial resolution than microwave or millimeter wave imaging, especially when used for a penetration depth of greater than 1 mm, which has not been achieved by infrared or optical imaging. A greater penetration depth would allow for a variety of applications, such as the nondestructive testing of industrial or farm products, or analyzing chemical composition by exploiting the spectroscopic feature. However, most THz imaging systems [e.g., THz time-domain spectroscopy (THz-TDS)] require prior mechanical adjustment to ensure that the focal point is on the target surface; this process narrows the possible measurement range along the depth direction, and such adjustment is hardly achieved if the depth of the object is unknown assumed in free space or subsurface depth imaging. Synthetic aperture (SA) approaches assuming wider beam observations, such as radar imaging, have thus been introduced to achieve automatic focusing at an arbitrary depth [1]. Researchers have investigated confocal submillimeter or THz-band radar imaging approaches in a variety of applications, including automotive terrain sensing [2], surface imaging [4], and personnel scanning systems [5]. However, SA approaches often provide blurred images along the depth direction, require high computational costs when obtaining full voxel images, and suffer from unnecessary responses to coherent processes, such as speckle, or side or grating lobe effects, which becomes more crucial in sparse array configurations.

As a promising alternative, the range points migration (RPM) method [6] has been developed to overcome a number of the limitations in SA imaging approaches, in terms of its accuracy and computational complexity. The RPM method is based on the incoherent conversion from the corrected time delays, so-called range point (RP) to their associated scattering centers with one-to-one correspondence. RPM allows auto-focusing if an accurate range profile is obtained by avoiding unnecessary responses. However, the original RPM, commonly uses a much wider radiation pattern to model electromagnetic wave propagation; this is not suitable for a typical THz-TDS observation model using a dielectric lens. This letter therefore aims to compensate for image distortion caused by out-of-focus effects and provides a more accurate target surface shape with lower computational costs, which is the main advantage over the SA process. This involves introducing an equivalent virtual source located at a focal point, as introduced by Matsui and Kidera [7]. The original RPM is then appropriately extended to the dielectric lens model with a straightforward manner. As a notable feature of the proposed RPM, it allow for investigation of far- and near-range (i.e., deeper and shallower from the focal point, respectively) situation alike. The experimental data measured by THz-TDS measurements demonstrate that the proposed RPM method accurately compensate the image distortion due to out-of-focus effects, which contribute to enhance the accuracy for target surface reconstruction with much lower computational complexity than those by the SA process.

II. Observation Model

The observation model used is shown in Fig. 1, where the transmitting source and receiving sensor are located at the same position on $z = 0$ plane to allow a reflection of the electric field to be recorded. $s(\boldsymbol{L}, R)$ denotes an output of range extraction filter (e.g., matched filter), using a reference signal, where $\boldsymbol{L} = (X, Y, 0)$ denotes the location of the source, $R = \mathrm{c}t/2$ is expressed by time t, and c is the speed of light in the background media. The RPs determined by the local maxima of $s(\boldsymbol{L}, R)$ are defined as $\boldsymbol{q}_i = (X_i, Y_i, R_i)$.

III. Depth Imaging Method

A. SA Method

Some approaches based on the SA process have been developed to achieve an automatically focusing on the wide beam observation scenario. The SA is based on a coherent integration scheme for measured complex-valued signals to attain the desired azimuth resolution at arbitrary depth. This process is known as delay and sum (DAS) or beam-forming used in ultrasound or microwave or millimeter radar imaging. However, the resulting image often suffers from unnecessary

Manuscript received December 11, 2019; revised March 22, 2020; accepted April 24, 2020. This work was supported by Japan Science and Technology Agency (JST), Precursory Research for Embryonic Science and Technology (PRESTO), Japan, under Grant JPMJPR1771. *(Corresponding author: Shouhei Kidera.)*

Takamaru Matsui is with the Graduate School of Informatics and Engineering, University of Electro-Communications, Chofu 1828585, Japan.

Shouhei Kidera is with the Graduate School of Informatics and Engineering, University of Electro-Communications, Chofu 1828585, Japan, and also with Japan Science Technology Agency, PRESTO, Kawaguchi 332-0012, Japan (e-mail: kidera@uec.ac.jp).

Color versions of one or more of the figures in this letter are available online at http://ieeexplore.ieee.org.

Digital Object Identifier 10.1109/LGRS.2020.2991155

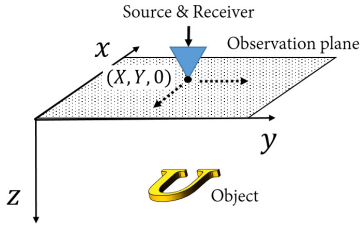

Fig. 1. Observation model.

responses because of the coherent integration process, such as speckle noise or grating- or sidelobe effects. In addition, the SA process requires an expensive computational cost to get a full 3-D image because it requires a large number of coherent integration process, using densely sampled data to avoid a false image due to sidelobe effect or speckle noise.

B. RP Migration Method

1) Original RPM Method: The RPM method has been developed to extract a target's boundary by exploiting a group of RPs. Each RP $\boldsymbol{q}_i$ is then converted to its associated scattering center point $\hat{\boldsymbol{p}}(\boldsymbol{q}_i)$ via the maximum likelihood approach for weighted kernel density estimators. This is formulated as

$$\hat{\boldsymbol{p}}(\boldsymbol{q}_i) = \underset{\boldsymbol{p}^{\text{int}}(\boldsymbol{q}_i,\boldsymbol{q}_l,\boldsymbol{q}_m)}{\arg\max} \sum_{j,k} g(\boldsymbol{q}_i;\boldsymbol{q}_j,\boldsymbol{q}_k) \times \exp\left\{-\frac{\|\boldsymbol{p}^{\text{int}}(\boldsymbol{q}_i;\boldsymbol{q}_j,\boldsymbol{q}_k)-\boldsymbol{p}^{\text{int}}(\boldsymbol{q}_i;\boldsymbol{q}_l,\boldsymbol{q}_m)\|^2}{2\sigma_r^2}\right\} \quad (1)$$

where $\boldsymbol{p}^{\text{int}}(\boldsymbol{q}_i,\boldsymbol{q}_l,\boldsymbol{q}_m)$ represents the intersection point for the three migration surfaces, each expressed as an orbit of possible propagation paths. In the case of free space, and the omni-directional transmitter and receiver with the same position, the migration surface becomes a spherical surface with radius R_i and the center $(X_i, Y_i, 0)$ [6]. σ_r is constant. $g(\boldsymbol{q}_i;\boldsymbol{q}_j,\boldsymbol{q}_k)$ is a weight function considering the sensor separation and reflection strength as

$$g(\boldsymbol{q}_i;\boldsymbol{q}_j,\boldsymbol{q}_k) \equiv |s(\boldsymbol{q}_j)| \exp\left\{-\frac{D_{XY,i,j}^2}{2\sigma_{XY}^2}\right\} + |s(\boldsymbol{q}_k)| \exp\left\{-\frac{D_{XY,i,k}^2}{2\sigma_{XY}^2}\right\} \quad (2)$$

where $D_{XY,i,j} = ((X_i - X_j)^2 + (Y_i - Y_j)^2)^{1/2}$. σ_{XY} is constant. $g(\boldsymbol{q}_i;\boldsymbol{q}_j,\boldsymbol{q}_k)$ weights the intersection points, which are generated by the vicinity around the focused RP $\boldsymbol{q}_i$. In general, the σ_{XY} of this Gaussian weight is set to a couple of sampling interval of sensors, and then, there is no need for calculating all the possible combinations of intersection points, because g exponentially decreases in more separated intervals. Also, if the sensor intervals are larger than R_i, the intersection point for $\boldsymbol{q}_i$, $\boldsymbol{q}_j$, and $\boldsymbol{q}_k$ would not exist, but those combinations should be eliminated in calculating (1). σ_{XY} can be determined by considering the assumed sampling interval of observation point [6].

Since the original RPM assumes the wide-beam propagation from the transmitter, this method is not necessarily required when using a dielectric lens because a migration surface is degenerated to a focal point. However, when the target is out-of-focus, a finite migration surface must be considered; thus, the RPM algorithm is still promising to attain a more accurate target boundary shape by compensating an image distortion due to the off-focusing effect.

2) Extended RPM Method With Virtual Source Model: An extended RPM model introducing a virtual source located at a focal point of the assumed dielectric lens to determine an appropriate migration surface was then designed. A similar idea for the SA process has been demonstrated in [1]. The distance between the lens surface and the focal point was defined as R_f, and R_i, defined in each RP $\boldsymbol{q}_i$, that denotes the distance between the lens and target surface, observed at the sensor location centered on $(X_i, Y_i, 0)$. As the THz beam is along the z-direction (i.e., the depth), the focal point for each sensor was to be defined as (X_i, Y_i, R_f). In the case of a far-range situation ($R_i > R_f$), the target surface was expressed as the outer envelope of the migration surfaces, each of which forms a spherical circumference with the center (X_i, Y_i, R_f) and the radius $|R_i - R_f|$ [8]; this is because an each equiphase surface forms a convex down one. Furthermore, in a near-range situation ($R_i < R_f$), a target boundary was expressed as an inner envelope of migration surfaces due to a convex-up equiphase surface. Fig. 2 shows the conceptual image for far and near range cases, where the equivalent source is denoted as (X_i, Y_i, R_f) and its migration surface becomes a spherical surface with center (X_i, Y_i, R_f) and radius $|R_i - R_f|$.

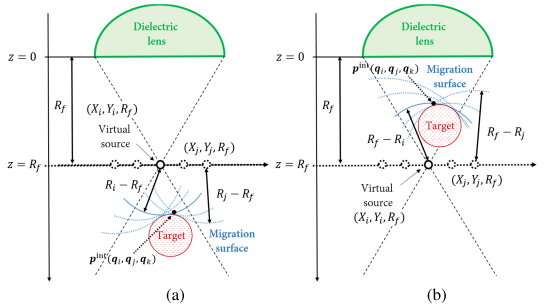

Fig. 2. Extended principle of the RPM method. (a) In a far range ($R_i > R_f$) case, a target surface is expressed as outer envelope of migration surfaces [spheres with the center (X_i, Y_i, R_f)]. (b) In a near range ($R_i < R_f$) case, a target surface is expressed as inner envelope of migration surfaces [spheres with the center (X_i, Y_i, R_f)].

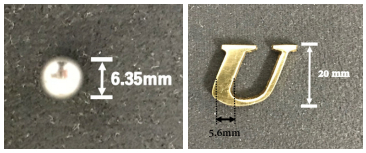

Fig. 3. Optical images of targets. (a) Metallic sphere with 6.35 diameter. (b) Alphabetical character "U."

The original RPM was thus extended to the dielectric lens model, where each RP $\boldsymbol{q}_i$ was converted as

$$\boldsymbol{q}_i \equiv (X_i, Y_i, 0) \rightarrow \tilde{\boldsymbol{q}}_i \equiv (X_i, Y_i, R_f). \quad (3)$$

Then, the scattered center point $\hat{\boldsymbol{p}}(\boldsymbol{q}_i)$ was determined as

$$\hat{\boldsymbol{p}}(\boldsymbol{q}_i) = \underset{\boldsymbol{p}^{\text{int}}(\tilde{\boldsymbol{q}}_i,\tilde{\boldsymbol{q}}_l,\tilde{\boldsymbol{q}}_m)}{\arg\max} \sum_{j,k} g(\tilde{\boldsymbol{q}}_i;\tilde{\boldsymbol{q}}_j,\tilde{\boldsymbol{q}}_k) \times \exp\left\{-\frac{\|\boldsymbol{p}^{\text{int}}(\tilde{\boldsymbol{q}}_i;\tilde{\boldsymbol{q}}_j,\tilde{\boldsymbol{q}}_k)-\boldsymbol{p}^{\text{int}}(\tilde{\boldsymbol{q}}_i;\tilde{\boldsymbol{q}}_l,\tilde{\boldsymbol{q}}_m)\|^2}{2\sigma_r^2}\right\}. \quad (4)$$

The existing area of each intersection point $\boldsymbol{p}^{\text{int}}(\boldsymbol{q}_i,\boldsymbol{q}_l,\boldsymbol{q}_m)$ should be $z > R_f$ when $R_i > R_f$ and $z < R_f$ when $R_i < R_f$. As in (1), the basic formulation in the extended RPM is the same except for the definition of the intersection point $\boldsymbol{p}^{\text{int}}(\boldsymbol{q}_i,\boldsymbol{q}_l,\boldsymbol{q}_m)$, it is a straightforward approach. As a notable advantage, this method achieves much lower computational complexity, when compared with the SA process by avoiding the use of a coherent integration process and calculating the number of the intersection points of spheres (analytically solved) to compensate the image distortions by off-focus effect.

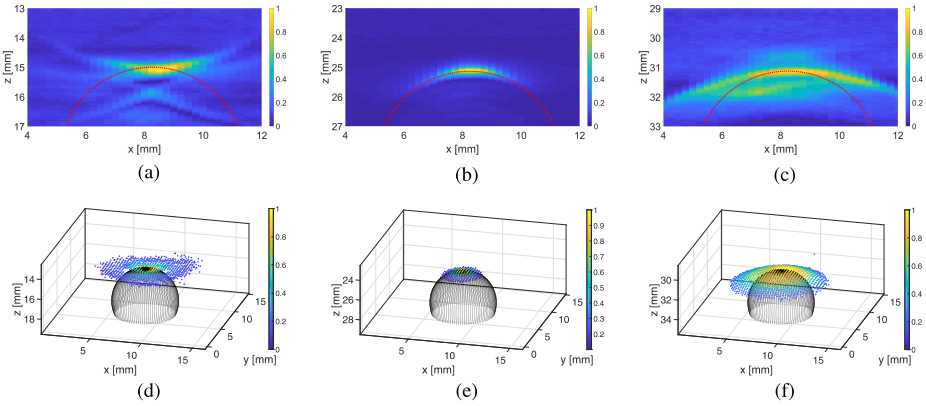

Fig. 4. Traditional THz-TDS depth images for the spherical metallic target at each depth. (a)–(c) Cross-sectional images. (d)–(f) 3-D images. Color denotes normalized signal strength. (a) and (d) Case 1. (b) and (e) Case 2. (c) and (f) Case 3.

Step 1): Signals are recorded at each set of transmitting and receiving sensor as $s(\boldsymbol{L}, t)$ and are processed by the range extraction filter, whose output is denoted as $s(\boldsymbol{L}, R')$.

Step 2): RPs are extracted as $\boldsymbol{q}_i$ from the local maxima of $s(\boldsymbol{L}, R')$ with respect to R', and converted to $\tilde{\boldsymbol{q}}_i$ as in (3).

Step 3): For each converted RP $\tilde{\boldsymbol{q}}_i$, the scattering center point $\hat{\boldsymbol{p}}(\boldsymbol{q}_i)$ is determined by (4).

Step 4): To attain a reconstruction accuracy, the following postprocessing is introduced. Herein, the following evaluation value is defined as:

$$\zeta(\hat{\boldsymbol{p}}(\boldsymbol{q}_i)) \equiv \sum_{j,k} g(\tilde{\boldsymbol{q}}_i; \tilde{\boldsymbol{q}}_j, \tilde{\boldsymbol{q}}_k) \times \exp\left\{-\frac{\|\boldsymbol{p}^{\text{int}}(\tilde{\boldsymbol{q}}_i; \tilde{\boldsymbol{q}}_j, \tilde{\boldsymbol{q}}_k) - \hat{\boldsymbol{p}}(\boldsymbol{q}_i))\|^2}{2\sigma_r^2}\right\}. \quad (5)$$

Namely, $\zeta(\hat{\boldsymbol{p}}(\boldsymbol{q}_i))$ denotes the maximized value of the right term in (4). Then, if the following condition is satisfied:

$$\zeta(\hat{\boldsymbol{p}}(\boldsymbol{q}_i)) \leq \beta \max_{\hat{\boldsymbol{p}}(\boldsymbol{q}_j) \in \mathcal{P}_i} \zeta(\hat{\boldsymbol{p}}(\boldsymbol{q}_j)) \quad (6)$$

the scattering center point $\hat{\boldsymbol{p}}(\boldsymbol{q}_i)$ is regarded as the isolated point, and is then removed from the final reconstruction image. Herein, the area $\mathcal{P}_i$ is defined as the inner space of the sphere with the center $\hat{\boldsymbol{p}}(\boldsymbol{q}_i)$ and the radius r_{th}, where r_{th} should be the order of the data sampling scale. β is constant value, satisfying $0 \leq \beta \leq 1$.

The reconstruction accuracy of the proposed method is basically independent of the depth to the target, neither near nor far range, which means that an autofocusing scheme was achieved at any depth.

IV. Results With Experimental Data

Experimental validation was then performed using a THz-TDS measurement system provided by Spectra Design Co., Ltd. The observation model is equivalent to that in Fig. 1. A photo conductive antenna with a dielectric lens with a diameter and focal length of 34 and 25 mm, respectively, was assumed and was scanned on the $z = 0$ plane with a fixed interval of 0.25 mm. The incident and reflection signals were emitted and recorded, respectively, at $(X_i, Y_i, 0)$. A pulse-modulated signal was assumed with 0.3-THz center frequency and 0.3-THz bandwidth. Three cases were investigated at three different target depths: 15 mm (Case 1), 25 mm (Case 2), and 31 mm (Case 3), where Case 2 represents an in-focus case. The Capon filter is applied to reduce unnecessary responses by range-sidelobe effect [9], and the reference signals are prepared using the reflection signal from large metallic plate at each depth in free space. In the RPM process, the parameters are set as $\sigma_{XY} = 0.25$ mm, $\sigma_r = 1.0$ mm, $\beta = 0.3$, and $r_{\text{th}} = 1.0$ mm.

A. Case in Spherical Shape

A spherical metallic ball with 6.35-mm diameter was first used to investigate the imaging performance of the proposed method as shown in Fig. 3. Fig. 4 shows the cross-sectional and the 3-D depth images obtained by the THz-TDS system for each case, where its optical image is shown in Fig. 3. The sphere was accurately illustrated with correct curvature in the in-focus image (i.e., Case 2), whereas the resulting images suffered from nonnegligible image distortions with incorrect curvature in Case 1 and Case 3. In particular, a concave shape was pictured for Case 1, that is, fatal for the 3-D imaging. The average *S/Ns* for each case were 33 dB for Case 1, 43 dB for Case 2, and 32 dB for Case 3, where the *S/N* is defined as the ratio of the maximum power of received signals to the average noise power in the time domain. On the contrary, Fig. 5 shows the depth images obtained by the extended RPM method at Case 1 and Case 3. It is noted that the THz-TDS depth image (discrete points) as Fig. 4 are input to the extended RPM as RPs $\boldsymbol{q}_i$, and it demonstrated that our proposed method accurately reconstructs the target surface with appropriate curvature by converting $\boldsymbol{q}_i$ (the THz-TDS depth points) to each associated scattering center as $\hat{\boldsymbol{p}}(\boldsymbol{q}_i)$ using (4). In addition, depth imaging obtained via SA for the Case 1 and 3 are shown in Fig. 6 and these images also correctly reconstruct the actual shape of the target by assuming the equivalent virtual source. However, 17 s were required to obtain only one cross-sectional image, where total calculation time to get full volumetric image is expected to greater than 500 s, while the RPM requires only 3 s to get a full 3-D image, using Intel Xeon CPU E3 1240 v5 3.50 GHz processor with 16-GB RAM. The above lower numerical complexity is from that the possible intersection points of spheres can be analytically solved in (4). Besides, we also confirmed that, at the case where a data sampling interval is greater than a half of wavelength (sparse sampling), a SA image suffers from false image due to sidelobe effect, while the RPM is free from these false images according to the incoherent process, which is also significant advantage of the proposed method. For a quantitative error analysis, the reconstruction error is defined as e, which is the minimum distance between the actual target boundary and each reconstructed point. The cumulative probabilities satisfying $e \leq 0.2$ mm, (0.2λ) are 6.9% and 10.1% for the traditional THz-TDS image at Case 1 [Fig. 4(a) and (d)] and Case 3 [Fig. 4(c) and (f)], respectively. On the contrary, those are 91.3% and 86.4% for the proposed method at

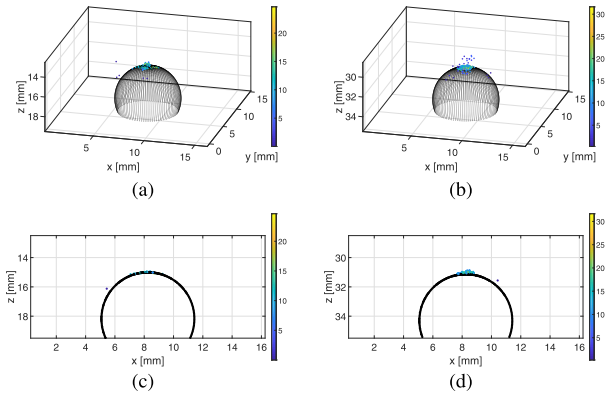

Fig. 5. Depth images obtained by the extended RPM method for the spherical metallic target at each depth. (a) and (b) 3-D view. (c) and (d) Sliced view. Black solid curves denote the true target boundary. Colored solid dots denote the scattering center points obtained by the proposed RPM, where its color level of each dot denotes ζ in (5). (a) and (c) Case 1. (b) and (d) Case 3.

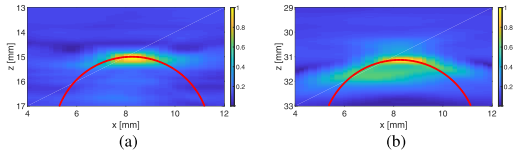

Fig. 6. SA images for the spherical metallic target at each depth. Color denotes normalized signal strength. (a) Case 1. (b) Case 3.

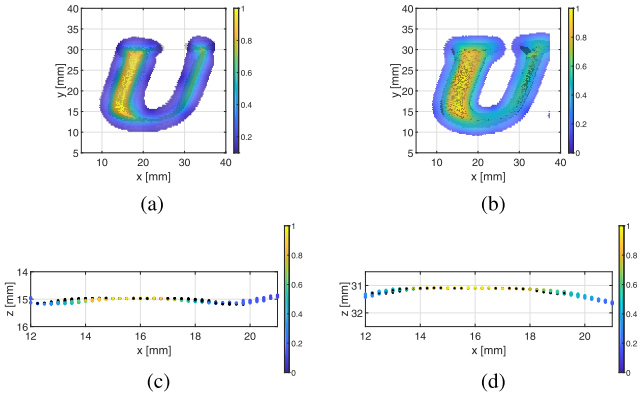

Fig. 7. Traditional THz-TDS depth images for the alphabetical "U" target at each depth. (a) and (b) Projected view on xy plane. (c) and (d) Sliced and expanded view on the left side of target. Color denotes normalized signal strength. (a) and (c) Case 1. (b) and (d) Case 3.

Case 1 [Fig. 5(a) and (c)] and Case 3 [Fig. 5(b) and (d)], respectively. This comparison verifies that the proposed RPM considerably enhances the reconstruction accuracy, especially for the out-of-focus case. It is noted that since the SA image offers a continuous distribution of reflection strength, which is different feature from that of the RPM (an aggregation of discrete points), its quantitative comparison is not introduced here to avoid an biased assessment. Qualitatively, however, the shape estimation accuracies of the SA and the RPM images are almost the same level, but the SA requires much more computational complexity.

B. Case in Alphabetical "U" Shape

A metal target in a "U" shape was then studied to show the applicability of the proposed method on a more elaborate shape, the optical image is as shown in Fig. 3. Fig. 7 shows the traditional depth images at each depth. The average *S/Ns* for each case are 18 dB for Case 1, 32 dB for Case 2, and 20 dB for Case 3. As with the spherical target, the depth images from Case 1 and Case 3 were considerably deformed because of the deformed equiphase wavefront.

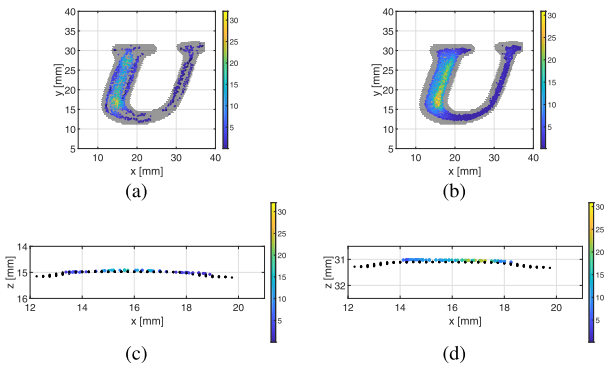

Fig. 8. Depth images obtained by the extended RPM method for the alphabetical "U" target at each depth. (a) and (b) Projected view on xy plane. (c) and (d) Sliced and expanded view on the left side of target. Color denotes ζ in (5). (a) and (c) Case 1. (b) and (d) Case 3.

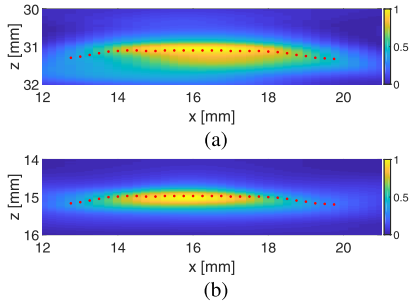

Fig. 9. SA images for the alphabetical "U" target at each depth. Cross section for same region in Fig. 8. Color denotes normalized signal strength. (a) Case 1. (b) Case 3.

TABLE I

CUMULATIVE PROBABILITY SATISFYING $e \leq 0.2$ mm

Target	Sphere		"U"	
Method	THz-TDS	RPM	THz-TDS	RPM
Case 1	6.9 %	91.3 %	64.1 %	99.0 %
Case 3	10.1 %	86.4 %	53.1 %	99.3 %

However, the RPM- or SA-reconstructed images accurately compensated the image distortion for all parts of the target, as shown in Figs. 8 and 9. Herein, the reference image was acquired at 25 mm (focal point). The cumulative probabilities satisfying $e \leq 0.2$ mm, (0.2λ) are 64.1% and 53.1% for the traditional THz-TDS image at Case 1 [Fig. 7(a) and (c)] and Case 3 [Fig. 7(b) and (d)], respectively. On the contrary, those are 99.0% and 99.3% for the proposed method at Case 1 [Fig. 8(a) and (c)] and Case 3 [Fig. 7(b) and (d)], respectively. Table I summarizes the error assessments for both target cases. It is noted that the reference image could not completely reconstruct the actual target shape, particular for the edge area of the character, namely, the diffraction effects from the edge incurs the expansion along the horizontal direction. Actually, the actual width for the cross-section area in Figs. 7–9 and is 5.6 mm, while that of the reference image is greater than the actual width due to edge diffraction effect. On the contrary, the RPM reconstructs the actual target width, by compensating the edge diffraction effect, in assessing the accumulation of the spherical migration curves in (4); this is one of the advantages of the RPM-based reconstruction. The above autofocusing feature is indispensable, especially for subsurface imaging, where the depth of covered target is generally unknown.

C. Case of Buried Target Into Hollow BOX

Finally, a subsurface scenario is made, where a target is buried in a hollow box and is investigated, and thus corresponds to a situation that an actual depth of a target

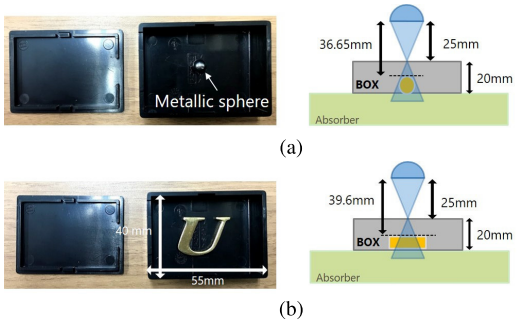

Fig. 10. Optical images of targets covered by plastic box and observation geometries. (a) Metallic sphere with 6.35 diameter. (b) Alphabetical character "U."

TABLE II

CUMULATIVE PROBABILITIES SATISFYING $e \leq 0.2$ mm THE CASE BURIED IN THE HOLLOW BOX

Target	Sphere		"U"	
Method	THz-TDS	RPM	THz-TDS	RPM
	28.5 %	82.2 %	30.4 %	53.6 %

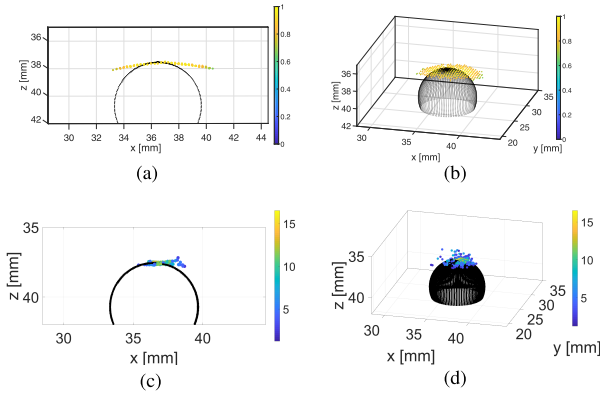

Fig. 11. Three-dimensional depth images for the spherical metallic target buried in hollow box. (a) and (b) Traditional THz-TDS images. (c) and (d) Extended RPM images. Color in (c) and (d) denotes ζ in (5).

surface is unknown. By assuming a thin thickness for dielectric box, it is expected that its time-delay in propagating into a media would not greatly affect an imaging accuracy by the proposed method. Fig. 10 shows the setup and geometric images for each target case buried in a plastic hollow box, which has a 40-mm width, 20-mm height, 55-mm depth, and 2.0-mm thickness at its upper lid. The focal point of the THz-TDS is set at the upper surface of the plastic box. Herein, we prepare the same reference signal model at each depth in free space. Figs. 11 and 12 show the comparison between the traditional THz-TDS image and the reconstruction image by the proposed method at each target case, where $\sigma_{XY} = 0.5$ mm is set. Table II summarizes the quantitative error analysis in this case. These results also demonstrated that our proposed method correctly reconstructs the actual target surface, while the THz-TDS images are seriously distorted from the actual target shape.

V. CONCLUSION

This letter presents an extended RPM method using a virtual source model to achieve automatic image compensation for a distorted image measured at a depth that is out-of-focus in the THz-TDS system. This method was shown to compensate for the distortion seen at depths both shallower and deeper than the focal point by extracting the outer and inner envelopes of the

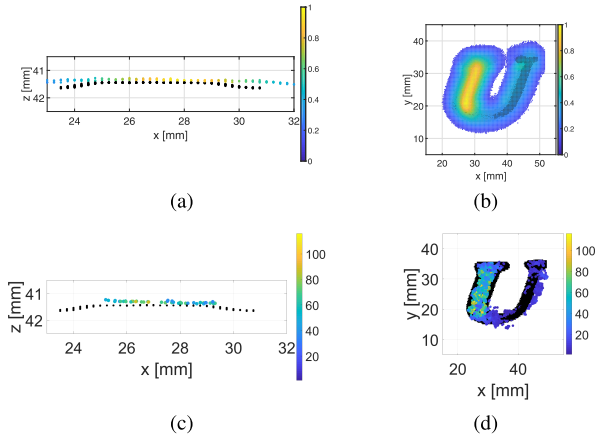

Fig. 12. Three-dimensional depth images for the alphabetical "U" target buried in hollow box. (a) and (b) Traditional THz-TDS images. (c) and (d) Extended RPM images. Color in (c) and (d) ζ in (5).

migration surfaces. Experimental validation using THz-TDS data for both free-space and subsurface scenario demonstrated that the proposed method provided more accurate 3-D images, even at out-of-focus depths, and required much less computational complexity than that by the traditional SA processing. In the case of narrower fractional bandwidth, the SA has an advantage for azimuth resolution using the coherent process, while the azimuth resolution of the RPM imaging relies on an accurate estimation of RPs, which becomes difficult in dealing with a narrower frequency band, and that is one of the disadvantages of the proposed method. Few of these challenges were solved in the other studies in [10], but rather requires several fast Fourier transform (FFT) processes, which would incur more computational cost than the proposed RPM.

REFERENCES

[1] S. C. Henry, "Three-dimensional broadband terahertz synthetic aperture imaging," *Opt. Eng.*, vol. 51, no. 9, May 2012, Art. no. 091603.

[2] D. Jasteh, E. G. Hoare, M. Cherniakov, and M. Gashinova, "Experimental low-terahertz radar image analysis for automotive terrain sensing," *IEEE Geosci. Remote Sens. Lett.*, vol. 13, no. 4, pp. 490–494, Apr. 2016.

[3] S. Palm, R. Sommer, and U. Stilla, "Mobile radar Mapping—Subcentimeter SAR imaging of roads," *IEEE Trans. Geosci. Remote Sens.*, vol. 56, no. 11, pp. 6734–6746, Nov. 2018.

[4] Y. Jiang, H. Wang, Y. Qin, B. Deng, J. Gao, and Z. Zhuang, "A three-dimensional surface imaging method using THz dual-frequency interferometry," *IEEE Geosci. Remote Sens. Lett.*, vol. 13, no. 11, pp. 1651–1655, Nov. 2016.

[5] S. Gu, C. Li, X. Gao, Z. Sun, and G. Fang, "Three-dimensional image reconstruction of targets under the illumination of terahertz Gaussian Beam—Theory and experiment," *IEEE Trans. Geosci. Remote Sens.*, vol. 51, no. 4, pp. 2241–2249, Apr. 2013.

[6] S. Kidera, T. Sakamoto, and T. Sato, "Accurate UWB radar three-dimensional imaging algorithm for a complex boundary without range point connections," *IEEE Trans. Geosci. Remote Sens.*, vol. 48, no. 4, pp. 1993–2004, Apr. 2010.

[7] T. Matsui and S. Kidera, "Accurate terahertz three-dimensional subsurface imaging by range points migration method," in *Proc. 44th Int. Conf. Infr., Millim., Terahertz Waves (IRMMW-THz)*, Sep. 2019, pp. 1–2.

[8] S. Kidera, T. Sakamoto, and T. Sato, "High-resolution and real-time 3-D imaging algorithm with envelopes of spheres for UWB radars," *IEEE Trans. Geosci. Remote Sens.*, vol. 46, no. 11, pp. 3503–3513, Nov. 2008.

[9] S. Kidera, T. Sakamoto, and T. Sato, "Super-resolution UWB radar imaging algorithm based on extended capon with reference signal optimization," *IEEE Trans. Antennas Propag.*, vol. 59, no. 5, pp. 1606–1615, May 2011.

[10] Y. Akiyama and S. Kidera, "k-space decomposition based range points migration method for millimeter wave radar," in *Proc. IEEE Int. Geosci. Remote Sens. Symp.*, Jul./Aug. 2019, pp. 680–683.